NeuroImage 198 (2019) 44–52

Contents lists available at ScienceDirect

NeuroImage

journal homepage: www.elsevier.com/locate/neuroimage

Microelectrode array electrical impedance tomography for fast functional imaging in the thalamus

Danyi Zhu [a], Alistair McEwan [a], Calvin Eiber [b,c,d,*]

[a] School of Electrical and Information Engineering, The University of Sydney, Camperdown, NSW, Australia
[b] Save Sight Institute, The University of Sydney, 8 Macquarie St, Sydney, NSW, Australia
[c] School of Medical Sciences, University of Sydney, Sydney, NSW, Australia
[d] Australian Research Council Centre of Excellence for Integrative Brain Function, Australia

ARTICLE INFO

Keywords:
EIT
Conductivity
Visual thalamus
Depth electrodes
Brain imaging
Modelling

ABSTRACT

Electrical Impedance Tomography (EIT) has the potential to be able to observe functional tomographic images of neural activity in the brain at millisecond time-scales. Prior modelling and experimental work has shown that EIT is capable of imaging impedance changes from neural depolarisation in rat somatosensory cortex. Here, we investigate the feasibility of EIT for imaging impedance changes using a stereotaxically implanted microelectrode array in the thalamus. Microelectrode array EIT was simulated using an anatomically accurate marmoset brain model. Impedance imaging was validated and detectability estimated using physiological noise recorded from the marmoset visual thalamus. The results suggest that visual-input-driven impedance changes in visual subcortical bodies within 300 μm of the implanted array could be reliably reconstructed and localised, comparable to local field potential measurements. Furthermore, we demonstrated that microelectrode array EIT could reconstruct concurrent activity in multiple subcortical bodies simultaneously.

1. Introduction

Electrical Impedance Tomography (EIT) is an emerging technique for imaging the activation of neural tissue in the brain over millisecond time-scales (Aristovich et al., 2014, 2016; Oh et al., 2011; Davidson et al., 2010). Recent advances in neural EIT have shown that epicortical arrays are capable of imaging sensory evoked activity by reconstructing changes in local tissue impedance throughout much of the cortex (Aristovich et al., 2016). The spatiotemporal resolution of EIT is fine enough to trace the transmission of information across columns and between layers in rodent cortex (Aristovich et al., 2016) using planar epicortical arrays. In this, neural EIT has begun to outperform the most comparable neuroimaging technique, EEG inverse source modelling. Neural EIT with planar epicortical arrays has not, however, been found to be effective for reconstructing impedance changes in deeper brain structures, such as the thalamus (Faulkner et al., 2018a).

Traditionally, EIT has been used for applications such as thoracic imaging of the lung and heart, where the measurement electrodes lie along the external surface of the volume to be imaged (Bayford, 2006). Sequences of electrode pairs are chosen for current injection, and the potential distribution arising from the applied current is measured on other electrodes on the array. By collecting ensembles of these potential distributions, images of the local spatial tissue impedance changes can be reconstructed. For fast neural EIT, the impedance changes of interest are due to ion channels in cell membranes opening during action potential initiation and propagation, and measured values of the expected tissue conductivity change range from 0.06% to 1.7% (Liston et al., 2012; Faulkner et al., 2018a; Faulkner et al., 2018b). Systems are currently under development which integrate both boundary electrodes and electrodes placed within the imaging volume to improve the spatial resolution of EIT, such as for the localisation of deep epileptic foci (Witkowska-Wrobel et al., 2018; Jeong et al., 2014).

In principle, EIT images can also be reconstructed from currents injected through small implanted microelectrode arrays, sacrificing non-invasiveness for the ability to resolve changes occurring in deep brain structures. The measurement of EEG-like signals, local field potentials (LFPs), in the deep brain is also confounded by a lack of anatomical regularity which is necessary for the generation of strong LFPs (Makarova et al., 2014; Buzsáki et al., 2012). Neural EIT circumvents this issue by measuring impedance changes, avoiding the issue wherein the summation of positive and negative membrane currents results in zero net signal. Without a strong theoretical framework for the interpretation of

* Corresponding author. Save Sight Institute, The University of Sydney, 8 Macquarie St, Sydney, NSW, Australia.
E-mail address: calvin.eiber@sydney.edu.au (C. Eiber).

https://doi.org/10.1016/j.neuroimage.2019.05.023
Received 23 January 2019; Received in revised form 26 April 2019; Accepted 9 May 2019
Available online 17 May 2019

thalamic LFPs, the need to develop neural imaging techniques with good spatial and temporal resolution which are suitable for work in the deep brain is even more pressing. Such a tool will be useful for applications such as deep brain implants, which are commonly used to treat Parkinsons disease (Benabid et al., 1996; Miocinovic et al., 2013) and are being investigated for the treatment of other neurological and psychological disorders (Miocinovic et al., 2013; Mayberg et al., 2005; Sturm et al., 2003).

This paper has two principal aims. The first is to quantify accuracy and sensitivity of microelectrode array EIT for reconstructing localised impedance changes which occur in the neighborhood of a probe microelectrode array, using a simplified spherical mesh and small spherical perturbations. The second is to investigate the feasibility of imaging the activation of different irregularly-shaped thalamic nuclei using a single electrode array. The primate thalamic visual nuclei lie in close proximity to one another in the thalamus and we are particularly interested in the physiology of visual processing, so we simulated impedance changes in the lateral geniculate nucleus (LGN), thalamic reticular nucleus (TRN), and inferior pulvinar (iPul) of the thalamic visual system of the common marmoset, *Callithrix jacchus*.

2. Methods

This section is structured as follows: As this is primarily a simulation study, we begin with a description of the EIT forward model (from which the data was generated) and inverse models (from which reconstructed images were generated for analysis). This is followed by a description of the simulated EIT measurement protocol. Measurements of physiological noise were undertaken in marmosets, and so the details of the *in-vivo* experiments and data acquisition are provided, along with equations for stationary multiplicative noise. The algorithms for EIT image reconstruction and perturbation localisation are outlined, and finally we present the details for an image post-processing algorithm to remove regularisation artefacts from the reconstructed images.

2.1. EIT forward and inverse models

In order to determine the accuracy and sensitivity of microelectrode array EIT, a 5 mm diameter, 577k-element spherical mesh with tetrahedral elements was generated using Comsol (COMSOL AB, Sweden, V5.1) centred on a simulated microelectrode array (NeuroNexus), as shown in Fig. 1A. Forward solutions for the potential distributions given the injected current were computed in Matlab 2Ω017a (Mathworks) on the University of Sydney Artemis HPC system. The simulated electrode array consisted of 32 electrodes (15 μm diameter, modelled as point electrodes) on two shanks of 16 electrodes each; the electrode spacing is 50 μm and the shanks are separated by 500 μm, and the mean electrode impedance was measured at roughly 600 kΩ at 1 kHz when the physiological noise was measured in absence of current injection. The simulated spherical volume was assigned a uniform conductivity of 0.15 Ωm^{-1} (Gabriel et al., 2009). A 0.2 mm diameter spherical conductivity perturbation increase of 1% (Aristovich et al., 2014) was simulated at each location in a 21 × 21 grid up to 1 mm away from the simulated electrode array in each direction in the plane of the electrode array. The optimal element size was determined using mesh convergence error method; the finest element size was 50 μm near the electrode with a mean volume growth rate of 1.6 towards the mesh boundary. Element quality was assessed according to the metrics proposed by Joe and Liu (Liu and Joe, 1994) with minimum element quality 0.527 and average quality 0.887. Images were reconstructed using a 5 mm diameter circular 2D mesh consisting of 25k elements with minimum element quality 0.582 and average quality 0.977.

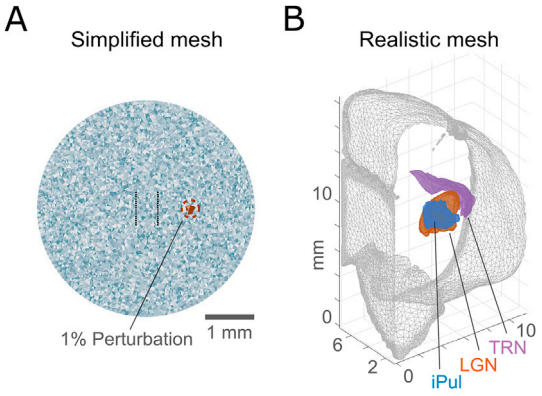

Fig. 1. EIT forward simulation meshes. A: cross-section through the 3-D spherical forward model mesh, demonstrating the mesh element size with an example perturbation. B: Three-dimensional realistic brain mesh for the marmoset brain, showing the relative location of the LGN, the TRN, and iPul.

To determine the feasibility of microelectrode array EIT to visualise impedance changes arising from irregularly-shaped thalamic nuclei, a realistic model of the marmoset brain was extracted from an anatomical atlas of the brain of the common marmoset, *Callithrix jacchus* (Paxinos et al., 2012) using custom software written in Matlab. Outlines of the TRN, LGN, iPul and ventricles were traced from sequential nissel-stained sections separated by 0.2–0.3 mm, and the resulting surface meshes were simplified and re-meshed using MeshMixer (Autodesk). The gray matter and white matter of the brain were assigned a uniform conductivity of 0.15 Ωm^{-1}, and the ventricles were assigned a uniform conductivity of 1.79 m^{-1} (Gabriel et al., 2009; Jehl et al., 2016). The final simulated bodies are shown in Fig. 1B. EIT measurements were simulated at a variety of electrode array positions, as shown in Fig. 2A, in the visual thalamus. Simulated measurements were taken for a 1% change in impedance in each of the LGN, TRN and iPul. In order to investigate the ability of microelectrode array EIT to differentiate multiple simultaneous inputs, simultaneous changes of 0.5% and 1% in two bodies simultaneously were also simulated. Changes were simulated throughout the whole body of the LGN, the TRN, and iPul.

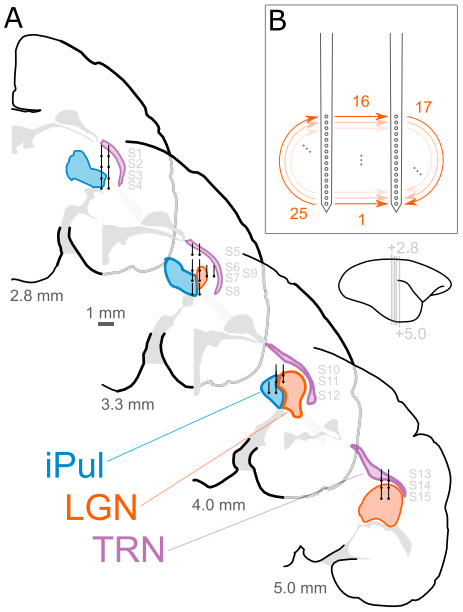

Fig. 2. Simulated microelectrode array locations and measurement pattern. A: 15 microelectrode array positions were simulated at a variety of locations in the visual thalamus, shown in serial coronal sections. Colored regions show the extent of the LGN, the TRN, and iPul; shaded regions show ventricles. Site numbers (referenced in Figs. 5, 8, and 10) are indicated in gray. B: measurement pattern for injected current through the microelectrode array. In total, 32 measurement patterns are applied, for a total of 870 measurements per reconstruction.

2.2. EIT measurement protocol

The performance of fast neural EIT depends on the pattern of injected probe currents and measurement electrodes. For naïve imaging, each electrode pair is measured, leading to a redundant set of measurements. However, if the region of interest is known, a subset of pairs can be chosen which maximise the current density in the region of interest while reducing the overall image acquisition time (Faulkner et al., 2017). The pattern of injection currents which we used is shown in Fig. 2B. In total, 32 measurement patterns are applied, for a total of 870 measurements per reconstruction (referenced to the top left electrode of the array). We also investigated the effects of adding a single external measurement electrode at various positions; the results of this exploration are presented in Supplementary Fig. S1.

We simulated a probe current of 10 μA at 1.45 kHz, roughly the maximum current allowable given the simulated electrode array. This current level was chosen to maximise sensitivity while minimising the risk of adverse electrochemical effects or inadvertent tissue activation. The most important factor for evaluating electrochemical safety is charge density per phase ($\mu C/cm^2$) (Rose and Robblee, 1990; Brummer and Turner, 1977; Eiber et al., 2013; McCreery et al., 1990). Based on the small electrode area of the simulated array (177 μm^2) and the maximum charge density for an optimal electrode material, activated iridium (3500 $\mu C/cm^2$ (Cogan et al., 2009)), no more than 6.2 nC/phase may be injected by the simulated microelectrode array EIT system. This limits the maximum probe current to 28.2 μA at 1.45 kHz. Additionally, injected currents as low as 4 μA at 250 Hz can cause activation of cells near an implanted microelectrode (Histed et al., 2009), artificially modifying the measured neural response. However, cell excitation thresholds increase with frequency (Reilly, 2002; Couto and Grill, 2016; Birdno and Grill, 2008), and the sinusoidal currents used for EIT are less efficient than square-wave pulses for neural stimulation (Sahin and Tie, 2007).

2.3. EIT background noise measurement

The inverse problems in EIT are highly sensitive to noise in the measured signals. The recording hardware, the electrode-tissue interface, and physiological processes in the tissue itself each introduce noise in the measured transimpedances. In order to quantify the expected level of physiological measurement noise, we analysed recordings of local field potentials performed in the visual thalamus of the common marmoset, *Callithrix jacchus*. All procedures conformed to the Australian National Health and Medical Research Council (NHMRC) code of practice for the use and care of animals and institutional animal care and ethics committee at the University of Sydney, as well as the code of ethics of the World Medical Association (Declaration of Helsinki).

Briefly, animal preparation for array recording of LFPs was as follows: Animals were sedated with an intramuscular injection of Alfaxan (12 mg kg^{-1}, Jurox, NSW, AUS) and Diazepam (3 mg kg^{-1}, Roche, NSW, AUS). Anesthesia and analgesia were maintained by continuous intravenous delivery of Sufentanil citrate (6 - 0 $\mu g\ kg^{-1}h^{-1}$; Sufenta Forte, Janssen Cilag, Beerse, BEL). Depth of anesthesia was monitored by continuous electroencephalography and pulse oximetry (SurgiVet, OH, USA). The animal was artificially respired with a 60%/40% mixture of NO_2 - Carbogen (5% CO_2 in O_2) and head-fixed in a stereotaxic frame. A durotomy was made above the LGN and the LGN was located using fine, high-impedance recording electrodes (2–11 MΩ, FHC, ME, USA). A NeuroNexus array (NeuroNexus, MI, USA) was implanted in the LGN stereotaxically. Before implantation, the electrode was coated in DiI (Invitrogen, Mulgrave, Australia), which enabled the electrode array location to be reconstructed from histological brain sections. At the conclusion of recordings the animal was killed with an overdose of pentobarbitone sodium (80–150 mg kg^{-1}, i. v.). Post-euthanasia, the animal was perfused with physiological saline (0.9% NaCl) followed by 4% paraformaldehyde in 0.1 M phosphate buffer (PB, pH 7.4), and the brain was removed and stored in a solution of glycerol (20% in 0.1 M PB). After 3–5 days, the brain was sectioned and stained with Neurotrace (Life Technologies Australia N21480) for fluorescence. DiI-stained tracks and thalamic bodies including the layers of the LGN are clearly visible, allowing the reconstruction of the recording array positions as shown in Fig. 4A. Further details as to our experimental setup and visual stimulus environment may be found in (Pietersen et al., 2014; Tailby et al., 2010; Eiber et al., 2018), and additional detail on the histological reconstruction of the array recording locations maybe found in (Cheong et al., 2013; White et al., 1998).

Action potentials and LFPs were recorded using the Cerebus multichannel recording system (BlackRock Microsystems) and a CerePlex digitising headstage (input impedance > 10 GΩ, resolution 0.25 μV), digitised at a rate of 30k samples/s and saved for offline processing. Robust spike and LFP responses to visual stimulation stereotypical of the different layers of the LGN could be consistently observed; an example LFP response to a visual stimulus presented through the contralateral eye is shown in Fig. 4B (averaged over 100 presentations). As expected, the

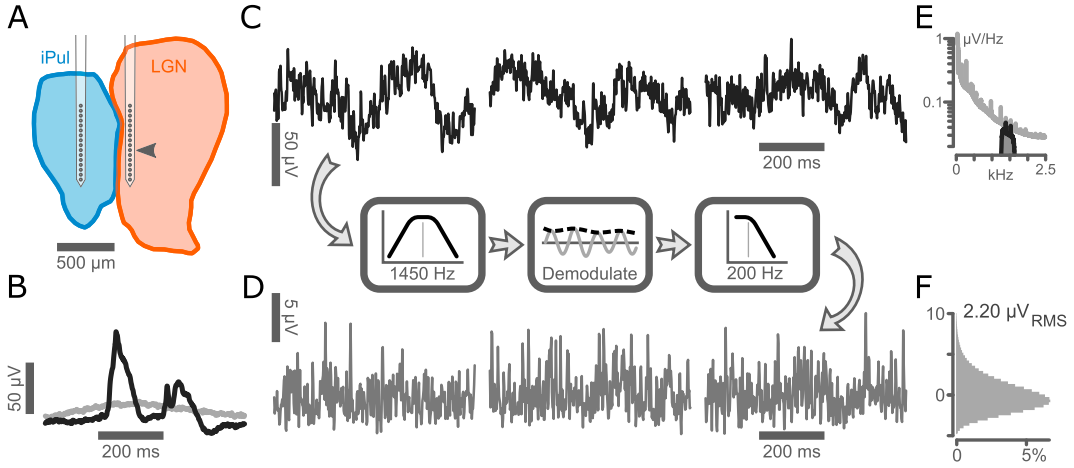

Fig. 3. Measurement of physiological and system noise. A: Histologically reconstructed microelectrode array placement in the visual thalamus. B: Example average visually evoked LFP for a visual stimulus presented through the contralateral eye (black) or no stimulus (gray). The source channel is indicated in A by the arrowhead. 100 stimulus presentations are averaged to reveal the evoked LFP. Stimulus duration is marked with a horizontal bar. C: Example individually recorded LFPs (0.7s duration) in the absence of stimulus, from the same channel as B. D: Residual power in the EIT measurement band centred on 1450 Hz for the example passes shown in C. This is the physiological component of the measurement noise. E: Overall spectrum of the measured LFPs (in gray), showing the 1/f characteristic of the LFP. The spectrum of the band-passed signal is shown in black. F: Overall distribution of the noise signal. The overall noise in this band is 2.20 μV_{RMS}.

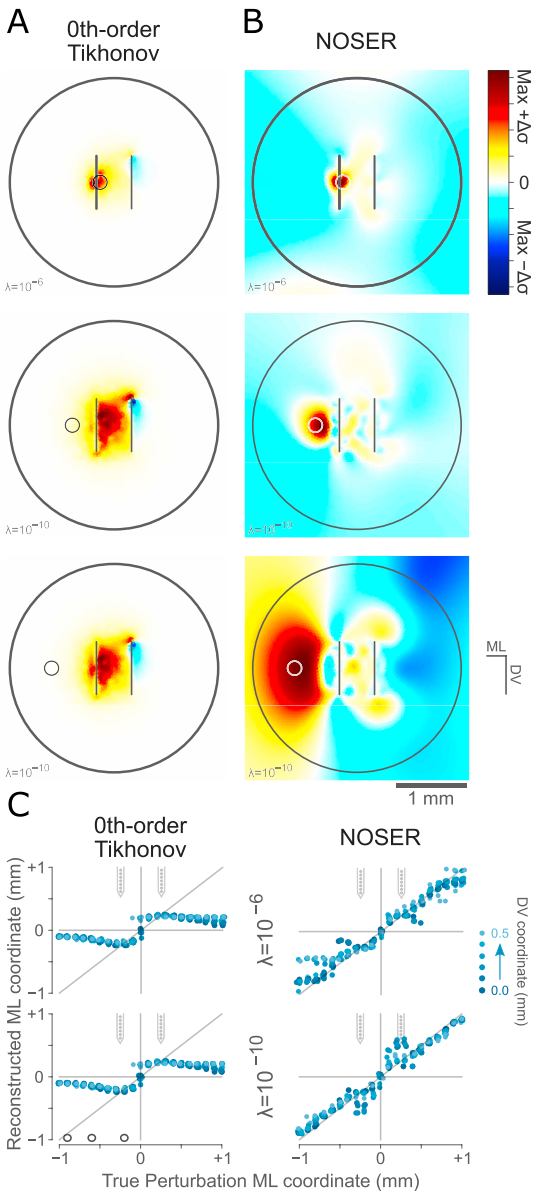

Fig. 4. Comparison of reconstructed perturbations with the NOSER and Tikhonov priors. A: Reconstruction using the Tikhonov prior for three perturbations along DV = 0 (indicated with circles) in the absence of noise. B: Reconstruction of same perturbations using the NOSER prior on the same mesh. Note the regularisation artifact in the bottom row. The 3 mm circular outline shows the extent of the grid of simulated perturbations, not the mesh boundary. C: Scatterplot of true vs reconstructed perturbation locations for $\lambda = 10^{-6}$ (top) and $\lambda = 10^{-10}$ (bottom). Cartoon array illustrates the array dimensions, and the positions of the perturbations illustrated in A-B are indicated with circles. Data point color indicates the distance of the perturbation from DV = 0, up to 0.5 mm.

frequency distribution of the LFPs follows a 1/f power law (Łeski et al., 2013), and so the physiological noise can be minimised by using probe currents of higher frequencies, greater than 1 kHz. To clarify, these were recordings of LFPs and single units only; we have not yet performed EIT measurements in-*vivo*.

In order to quantify the physiological noise which one would expect for microelectrode array EIT in the visual thalamus, the measured LFPs were band-pass filtered between 1250 and 1650 Hz (simulating a probe stimulus frequency of 1450 Hz and a temporal resolution of 5 ms), and the signal was demodulated using the Hilbert transform. The demodulated signal was then low-pass filtered for frequencies less than 200 Hz and down-sampled to a sampling rate of 500 Hz, as shown in Fig. 3D. The mean signal power in this band was estimated from a separate set of LFP traces and subtracted from the observed noise. The resulting noise waveforms had a RMS voltage of 2.2 μV. For the current injection pattern shown in Fig. 2B, a standard visual stimulus protocol (Pietersen et al., 2014) permits the averaging of three stimulus presentations per current injection pair. In order to simulate an EIT measurement with temporal resolution of 30 Hz (chosen to reflect the frequency content of a typical visual evoked potential), the mean of 48 noise samples (16 samples × 3 repeats) was added to the simulated transimpedance measurements. In practice, the trade-off between the noise level and the temporal resolution of the observed impedance changes can be adjusted during analysis based on the observed level of measurement noise. The geometry of the recording array was preserved during this process, such that correlations in the noise between different channels and small variations between the sensitivity of individual channels (which can introduce artefacts into the reconstructed images) were preserved.

Multiplicative noise arising from the current is often the limiting factor in EIT, as it is highly correlated on all electrodes and causes artefacts in the images. This is particularly pronounced in systems where the electrodes have a relatively high contact impedance, such as in microelectrode array EIT. In addition to the additive physiological noise, multiplicative noise (drawn from a normal distribution with $\sigma = 0.01\%$ (Jehl et al., 2016)) was added to the recordings, such that the overall potentials P_{total} were given by

$$P_{total} = P_{sim} * (1 + \xi_M) + P_{LFP} \quad (1)$$

where P_{total} is the final potential used for reconstructing conductivity images, P_{sim} is the solution to the detailed forward model, ξ_M is the multiplicative noise (averaged over 48 samples), and P_{LFP} is the measured physiological noise (averaged over 48 samples). P_{LFP} was randomised by using a different set of 48 samples (drawn from a set of 1050 possible measurement patterns) for each reconstruction. To assess whether the inter-channel differences in the physiological noise introduce significant artefacts, in some reconstructions P_{LFP} was replaced by normally distributed noise drawn from a normal distribution with $\sigma = 2\,\mu$V (averaged over 48 samples). Noise was added to both the measures of the homogeneous conductivity volumes and the perturbed conductivity volumes. Supplementary Fig. S2 shows the relative magnitude of the noise and the observed potential differences, as well as their relationship to the accuracy of perturbation localisation.

2.4. EIT image reconstruction

The spatial distributions of the impedance changes were reconstructed using EIDORS V3.8 (Adler et al., 2015). In order to reconstruct the change in impedance from the measured change in electrode potential (dP), the inverse problem was linearised and solved using the one-step Gaussian-Newton method:

$$dE = RM * dP \quad (2)$$

where dE is the reconstructed element-wise changes in impedance, dP is the difference in measured potential between the homogenous and perturbed conditions, and RM is the reconstruction matrix. RM is given in Wiener filter form by:

$$RM = \frac{PR^{-1} * J^T}{J * PR * J^T + \lambda I} \quad (3)$$

In equation (3), PR is the prior matrix (either the NOSER prior (Cheney et al., 1990) or 0th-order Tikhonov (Aristovich et al., 2014, 2016)), J is the Jacobian matrix (the linearised derivatives of the electrostatic equations of state) and λ is the regularisation hyperparameter.

The geometry of the inverse problem for microelectrode array EIT is substantially different from other applications of EIT; typically, in EIT,

the measuring electrodes are placed along the outer boundary of the volume of interest. However, in microelectrode array EIT, the electrodes are at the centre of the volume, and the goal is to reconstruct changes occurring beyond the extent of the electrode array. The quality of the reconstructed images depends on the chosen prior and regularisation hyper-parameter λ, but it is not yet well-known what parameters are best suited for reconstructing microelectrode array EIT.

To address this, we compared images generated using a 0th-order Tikhonov prior (the most commonly used prior for neural EIT (Aristovich et al., 2014; Aristovich et al., 2016)) and the NOSER prior (Cheney et al., 1990). These two priors encode different *a priori* assumptions about the perturbation size and shape. The 0th-order Tikhonov prior penalises large conductivity changes, but otherwise provides the fewest assumptions about the reconstructed image. The NOSER prior is an example of a Tikhonov-type regularisation method which tries to reguarlise sensitivity distribution to make the noise covariance uniform, and is suitable for reconstructing small conductivity perturbations in conjunction with the one-step Gaussian-Newton method. This non-iterative method is fast and provides accurate location information, but does not accurately reconstruct the absolute magnitude of conductivity perturbations. Accordingly, our results are displayed normalised to the maximum reconstructed conductivity change. Additionally the NOSER prior tends to reconstruct circular perturbations (even for perturbations of arbitrary shape) and can suffer from "mirror image" artifact surrounding the real perturbation (Cheney et al., 1990). As is shown in Fig. 4, only the NOSER prior was effectively able to reconstruct perturbations beyond the extent of the electrode array. A range of different values for λ were evaluated; Fig. 4 shows results for $\lambda = 10^{-6}$ and $\lambda = 10^{-10}$. Reconstructions with $\lambda = 10^{-6}$ gave more accurate results than $\lambda = 10^{-10}$ when the perturbation intersects the electrode array, and images reconstructed in the presence of noise using $\lambda = 10^{-6}$ consistently had the most reliable perturbation localisation in both the simplified spherical and anatomically realistic data-sets, but the overall results were not highly sensitive to our choice of λ. Using the L-curve technique for determining λ (Hansen, 2007) with λ from 7.2×10^{-3} to 4.8×10^{-20}, the optimum λ ranged from 1.0×10^{-8} to 2.0×10^{-5} (median 5.6×10^{-7}, see Supplementary Fig. S3).

2.5. Perturbation localisation

In order to quantify the reconstruction performance of different algorithms, the location of the perturbation was determined by identifying the largest connected cluster of elements greater then a threshold, defined as the average of the median element change and 50% of the maximum change (Malone et al., 2014; Jehl et al., 2016). The reconstructed perturbation location is approximated as the barycentre of this region of interest. The localisation error is then the distance between the true and the reconstructed perturbation, which we leave in units of mm. For reconstructions of realistic anatomy, the barycentre of the body of interest was calculated by exponentially discounting elements greater than 1 mm from the centroid of the electrode array. This technique is only applicable when the perturbed body intersects the plane of the electrode array, and was not applied when multiple areas were simulated simultaneously. Figs. 5 and 6 shows examples of regions of interest and their corresponding perturbation locations.

2.6. EIT image post-processing

While the NOSER prior is successful at reconstructing perturbations far from the electrode array, the regularisation introduces a saddle-shaped artifact to the image, which interferes with the localisation of changes as described above (as shown in Fig. 5). This artifact persists for all values of λ which permit the reconstruction of perturbations far from the electrode array. To remove this artifact, we apply the prior knowledge that the measured change in conductivity far from the electrode

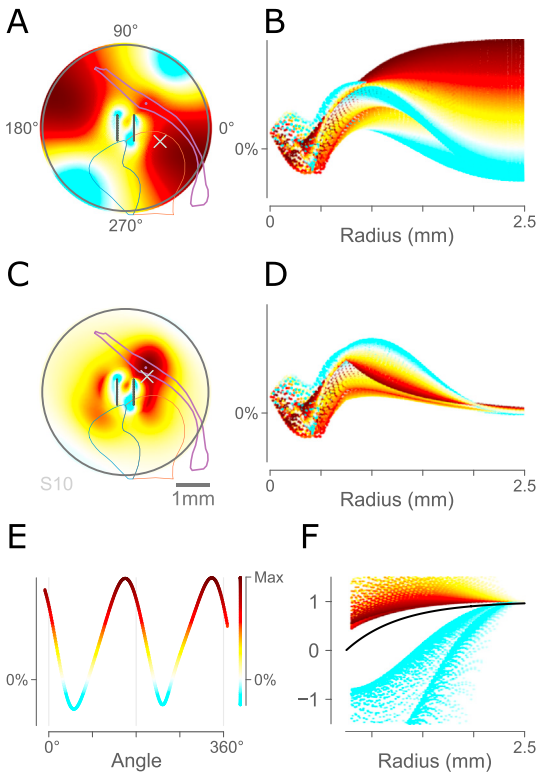

Fig. 5. Illustration of artifact subtraction. A: conductivity image for a 1% change in the TRN. TRN outline and anatomical barycenter are shown in purple, and estimated perturbation location is indicated with a white × . B: conductivity change as a function of radius. Data color corresponds to E_{img} at r_{max}. C: conductivity image after artifact subtraction. D: (as B). E: raw reconstructed boundary conductivities $E_{img}(r_{max}, \theta)$ as a function of θ (arbitrary scale). F: Fitted decay function $(1 - e^{r/r_0})$ (in black) and source data for fit, following the same coloring as E.

array is zero. The artifact is approximated (in circular coordinates) by the equation

$$E_{art}(r,\theta) = \begin{cases} (1 - e^{r/r_0}) E_{img}(r_{max}, \theta) & r > r_0 \\ 0 & r \leq r_0 \end{cases} \quad (4)$$

where the artifactual conductivity $E_{art}(r, \theta)$ at distance r and angle θ from the array is zero within radius r_0 and decays exponentially towards the observed boundary conductivity change $E_{img}(r_{max}, \theta)$ at angle θ. These parameters are fit post-*hoc* to each image using a standard non-linear least square method. This artifact technique is demonstrated in Fig. 5. In Fig. 5, the top row shows the raw reconstructed conductivity changes E_{img} in 2D and as a function of radius, the middle row shows the image after the *post hoc* artifact subtraction, and the bottom row shows $E_{img}(r_{max}, \theta)$ and the fitted values for $(1 - e^{r/r_0})$. Note how the estimated perturbation position is dominated by the NOSER artifact in Fig. 5A, but corresponds closely with the areas near the array undergoing changes in Fig. 5C. This procedure enables the localisation of perturbations in images which would otherwise be dominated by this regularisation artifact - this is particularly pronounced for small perturbations far from the electrode array, as in Fig. 6C.

3. Results

3.1. Validation

For our simplified sphere data, calculating the perturbation location after artifact removal significantly decreases the estimated position error ($p < 10^{-5}$, paired t-test), as illustrated in Fig. 6 using $\lambda = 10^{-10}$. In

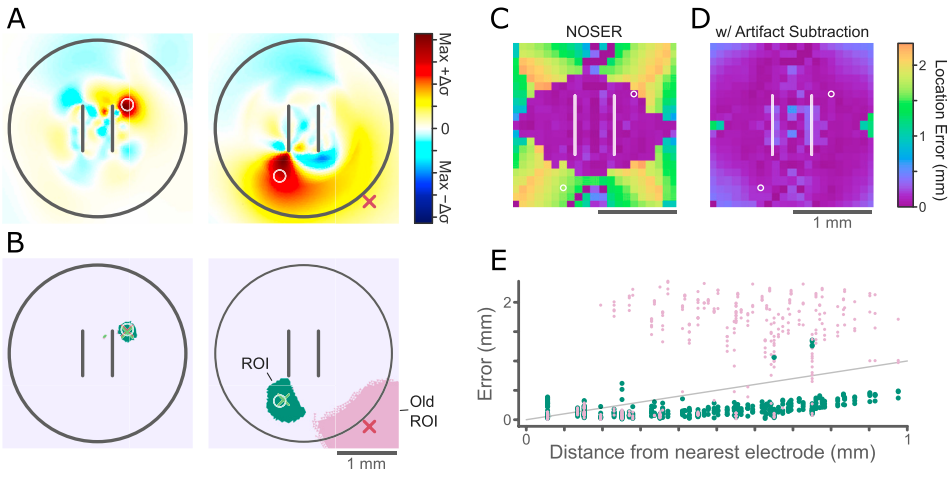

Fig. 6. Perturbation localisation. A: Reconstructed, artifact-subtracted changes in conductivity for two different perturbation locations, indicated with white circles, in the absence of noise. Left: the perturbation is close to the array, and the effects of artifact subtraction are minimal. Right: the perturbation is far from the array, and the effects of artifact subtraction are significant. B: thresholded regions of interest (ROIs) for perturbations shown in A. The dark green region shows the largest connected cluster of elements, and the pink area shows the suprathreshold elements for the raw conductivity image. The red and green Xs indicate the centroid before and after artifact subtraction, respectively. C: localisation error at every simulated perturbation location, relative to the electrode array in the absence of noise. Data shown in A,B indicated with circles. Darker colors indicate lower error; 1 pixel per 0.1 mm. D: localisation error after artifact subtraction. Localisation accuracy decreases only slightly with distance from the array. E: scatter-plot of localisation accuracy vs distance to the nearest electrode. Small light markers show localisation error calculated from raw NOSER image; dark green markers show localisation error calculated after artifact subtraction.

Fig. 6, post-processed reconstructions of the changes in conductivity (in the absence of noise) are shown for two different perturbation locations, as well as the perturbation regions of interest. When the location is calculated from the raw conductivity changes, a steep increase in location error is observed beginning 0.2 mm distant from the electrode array. These errors arise as the NOSER artifact dominates the central perturbation, as illustrated in Fig. 6A and B. With the artifact removed, the localisation error is significantly reduced, even for perturbations as far as 1 mm distant from the centre of the electrode array (Fig. 6D and E) in the absence of noise.

3.2. Noise sensitivity

The presence of noise significantly degrades the quality of the reconstructed EIT images ($p < 0.001$), as illustrated in Fig. 7 for $\lambda = 10^{-6}$. The magnitude of the reconstructed perturbation decreases with the distance from the microelectrode array to the true perturbation location, and for a 0.2 mm diameter perturbation is below the noise floor beyond 0.3 mm from the electrode array. The addition of multiplicative measurement noise to the physiological noise did not significantly worsen the localisation error ($p = 0.46$, 4-way ANOVA corrected for multiple comparisons using Tukey's method). Localisation error under the addition of artificial, normally-distributed noise was not significantly different to that under physiological noise ($p = 0.95$), which suggests that the correlations in the noise between different channels and small variations between the sensitivity of individual channels do not introduce additional artefacts into the reconstructed images. For perturbations within 0.3 mm of the array, there was no significant difference in localisation performance in the presence of noise ($p \geq 0.31$, 4-way ANOVA). Reconstruction of changes in the anatomically realistic mesh were less sensitive to the addition of noise ($p = 0.24$, paired t-test).

3.3. Realistic subcortical bodies

Fig. 8 shows reconstructed images of the conductivity changes in the LGN, the TRN, and in iPul from a variety of electrode positions reconstructed in the presence of noise (physiological + 0.01% multiplicative) with $\lambda = 10^{-3}$. The top row shows reconstructed activity in each of the LGN, the TRN, and iPul in response to a 1% change throughout each of those bodies. From a single array position, activity in each of these bodies can be tracked in the presence of noise. When the electrode array passes partially through the region of tissue undergoing the conductivity change, the electrodes lying within and outside the body can be readily distinguished from the reconstructed impedance image. This is demonstrated in the LGN (Fig. 8B), the TRN (Fig. 8F), and iPul (Fig. 8G), and can also be observed for reconstructions of concurrent activity in the LGN and iPul in Fig. 9. When the microelectrode array lies entirely within the region of change, a large-magnitude characteristic ring image is reconstructed; examples are shown with the array positioned entirely within the LGN and iPul (Fig. 8D,H). The reconstructed image is also sensitive to changes in conductivity out of the plane of the reconstruction; Supplementary Fig. S4 shows an example of a reconstruction of a change in LGN recorded posterior to the LGN. The artifact removal procedure can also sometimes obscure true changes (Fig. 8E,I); in that case, the NOSER image should be observed directly.

Fig. 9 shows the reconstructed changes in conductivity which are observed for concurrent changes in multiple areas, observed from a single array position. As with Fig. 8, images are reconstructed in the presence of noise (physiological + 0.01% multiplicative) with $\lambda = 10^{-6}$. Although the signals are not the same amplitude, the impedance changes in the LGN and in iPul can be readily and independently distinguished, even when both regions experience changes in impedance simultaneously. While the TRN can be localised in the presence of noise, the signal resulting from changes in the TRN is too weak to substantially affect the reconstructed images in the presence of signals from the LGN or iPul. This overall trend – that changes in different areas could be observed simultaneously, as long as the measured signals from those areas were similar in magnitude – was observed at all array positions.

4. Discussion

Microelectrode array EIT is a promising new technique for visualising neural activity in deep brain structures which are historically difficult to access (Faulkner et al., 2018a). The sensitivity and range of microelectrode array EIT, up to about 300 μm, is comparable to that of recording local field potentials; in the cortex, LFPs can theoretically spread up to several mm (Kajikawa and Schroeder, 2011), but in practice originate from sources within 200 μm of the recording electrodes (Łeski et al., 2013). In recording from subcortical structures, however, microelectrode array EIT has a number of advantages over LFP recording. First, recording

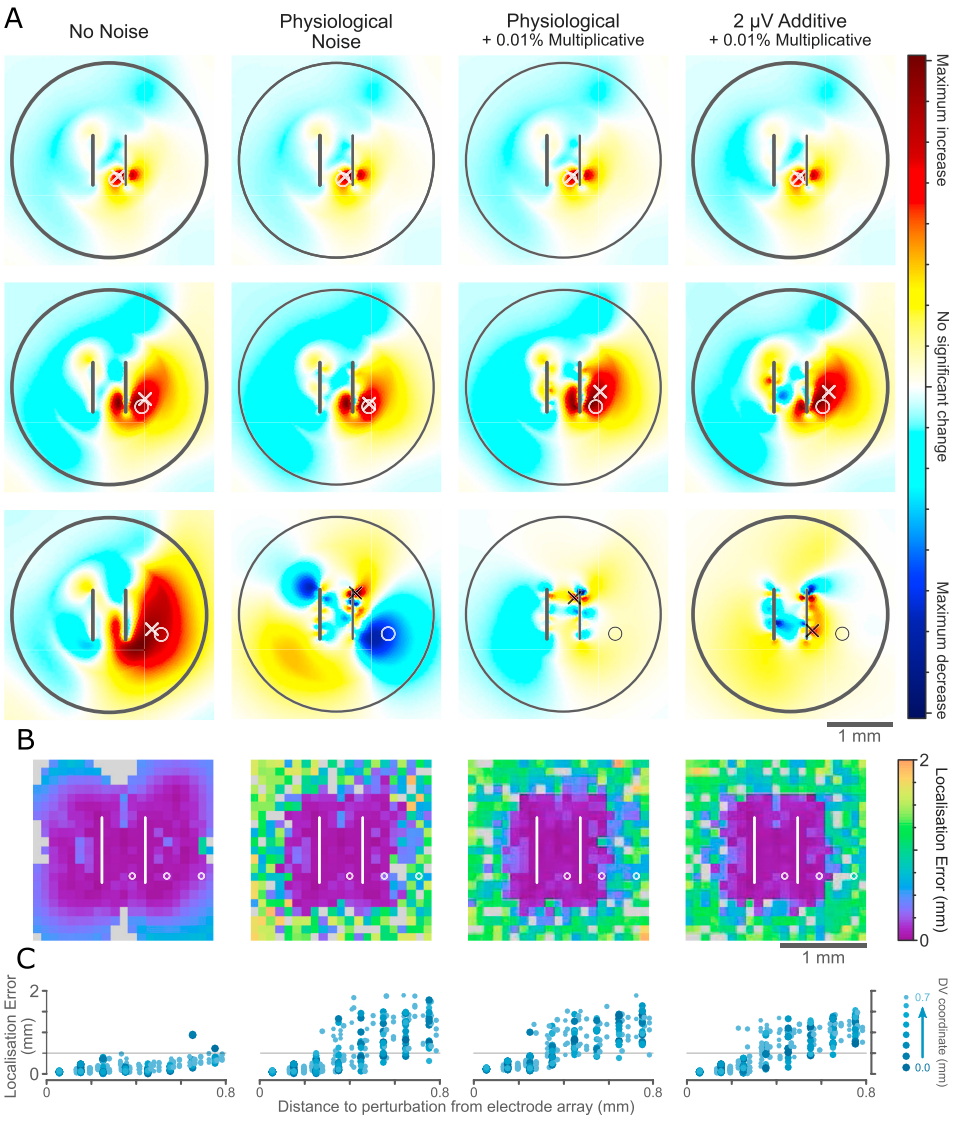

Fig. 7. Reconstructed conductivity images under the influence of noise. A: Example reconstructions for no noise, physiological noise (E_{LFP}) only, physiological and multiplicative noise, and fully artificial noise. B: Localisation error surfaces for all reconstructed perturbations following the style of Fig. 7C; Darker colors indicate lower error; gray pixels indicate that no perturbation was successfully reconstructed at that position. 1 px = 0.1 mm. C shows scatter-plots of the localisation error against perturbation position.

LFPs in subcortical structures is challenging, as LFP generators in the thalamus are complex multisource structures with heavy spatial overlap which lack the clear laminar organisation of cellular inputs and outputs found in the cortex or hippocampus (Makarova et al., 2014). EIT ameliorates this by recording impedance changes, which are not subject to cancellation through the superposition of positive and negative changes to the same extent as LFPs (Liston et al., 2012). Secondly, and more importantly, microelectrode array EIT allows for the reconstruction of the spatial distribution of the impedance changes. Inverse source modelling techniques to solve this problem have been developed for EEG (Grech et al., 2008), and approaches to this problem based on current source density (CSD) (Buzsáki et al., 2012) or independent component analysis (Makarov et al., 2010) have been proposed for LFPs, but these techniques cannot reproduce the spatial information present in microelectrode array EIT recordings (Supplementary Fig. S5 shows an example CSD map for an electrode positioned across the different layers of the LGN). While the methods used here only visualise relative impedance changes (and our results are normalised accordingly), other techniques using iterative image reconstruction techniques can also produce accurate estimates of the magnitude of the changes at the cost of additional computational complexity.

Our results demonstrate that, in the presence of realistic physiological and measurement noise, impedance changes in different subcortical structures can be distinguished. The ability to track the activity in multiple subcortical bodies simultaneously is important for studying phenomena such as attention, which for vision is most likely mediated through interactions between the TRN and the LGN and other, higher-order visual thalamic nuclei. Under normal visual stimulation, we would expect somewhat smaller regions activation than what we have simulated here. More cells in the LGN represent the fovea and perifoveal regions than the periphery, and so a visual scene spanning the first 7 of visual space viewed binocularly will activate about half of the LGN (roughly speaking, the posterior half (White et al., 1998)), and so activation of large percentages of the subcortical bodies under natural viewing conditions is not inconceivable.

These preliminary results are promising, although the development of dedicated image reconstruction algorithms for microeoectrode array EIT would doubtless improve upon what we have presented here. The impedance trajectory techniques used in the cortex by Aristovich et al. (Aristovich et al., 2016) will also be useful for visualising and tracking the flow of information between different subcortical bodies or between the thalamus and the cortex. Given a detailed conductivity map of the tissue, the inverse solution techniques of EIT can also be used to assist in the interpretation of local field potentials and other recorded signals. However, future work will have to prove that microelectrode array EIT is successful in-vivo; past predictions about the feasibility of fast neural EIT

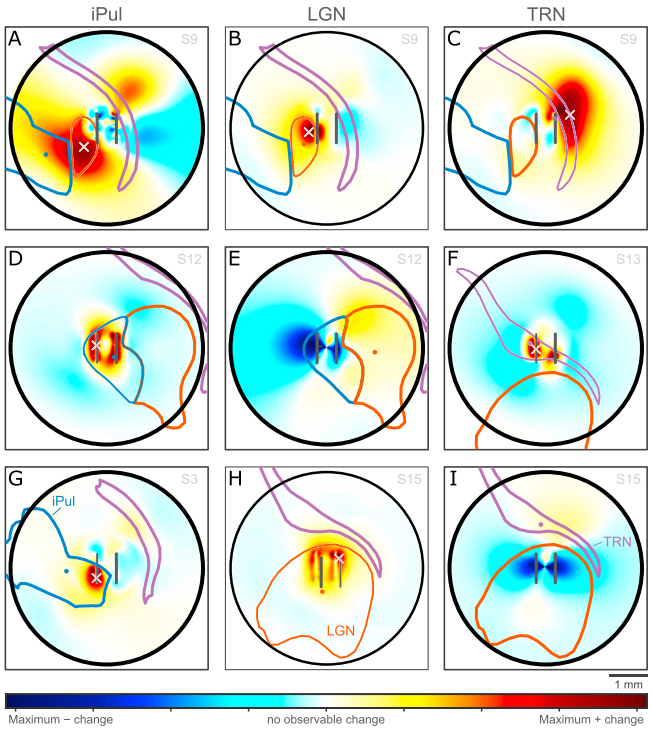

Fig. 8. Example reconstructed images for conductivity changes in various subcortical bodies. Outlines of the LGN, the TRN, and iPul are shown in red, purple, and blue, respectively. Barycenters are marked with a point and reconstructed locations with a white ×. All images are the same scale.

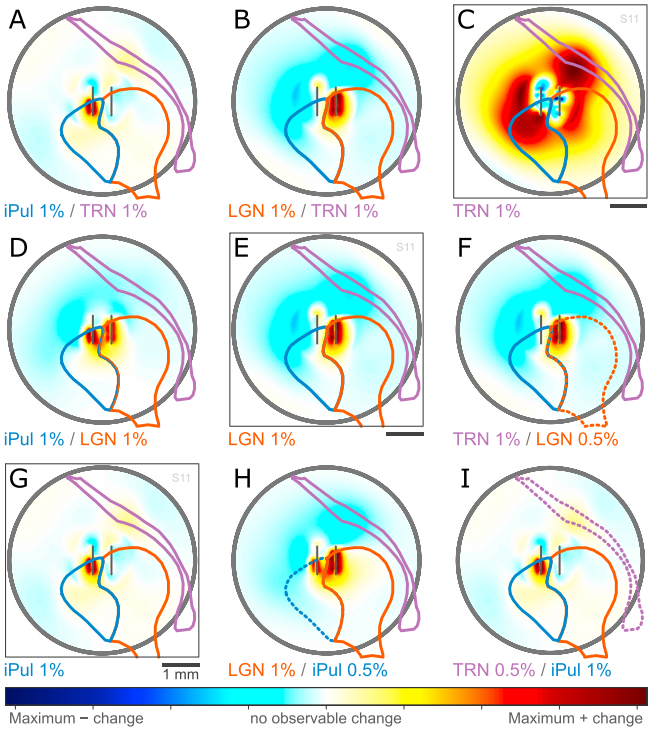

Fig. 9. Example reconstructed images for conductivity changes in various subcortical bodies. Outlines of the LGN, the TRN, and iPul are shown in red, blue, and purple, respectively.

(Aristovich et al., 2014) for imaging thalamic nuclei have turned out to underestimate the difficulty of resolving impedance changes in the deep brain, far from the recording electrode arrays (Faulkner et al., 2018a). It is also worth investigating the effect of the recording electrode geometry on the sensitivity of the reconstructed images, as well as exploring the reconstruction parameters which lead to optimal image estimation for microelectrode array EIT. Finally, little is currently known about how the impedance of neural tissue changes during periods of predominantly inhibitory input, as opposed to excitation and action potential propagation. Speculatively, it is possible that EIT may be able to differentiate structures that consist largely of inhibitory neurons (such as the TRN) from structures which consist primarily of excitatory neurons (such as the LGN), on the basis of the polarity of response or impedance frequency spectra; changes in different areas may also be distinguished by their latency of response. Similarly, regions with different calcium-binding mechanisms may also have different impedance spectra. More detailed biophysical and anatomical modelling is needed in order to address this question.

While recording with invasively implanted microelectrode arrays is a powerful tool used by neuroscience researchers, there are also significant potential clinical applications for EIT imaging in the deep brain. Deep brain stimulators are frequently implanted for the treatment of Parkinsons and other movement disorders (Benabid et al., 1996; Miocinovic et al., 2013), but are being investigated for the treatment of a wide range of psychiatric conditions including bipolar disorder (Gippert et al., 2017) and multiple-drug-resistant depression (Mayberg et al., 2005). The successful treatment of these conditions, as well as the prevention of unwanted side-effects, depends on the precise targeting of the therapeutic stimulus (Miocinovic et al., 2013; Sturm et al., 2003; Tan et al., 2013; Tamma et al., 2002), which can be achieved using field-shaping techniques (Butson and McIntyre, 2008; Contarino et al., 2014) after stereotaxic placement of the electrodes. The ability to visualise movement-, encapsulation-, and stimulus-related impedance changes near the stimulating electrode array would be of great utility to clinicians for tuning the stimulus parameters of individual patients' implants and would shed light on the underlying therapeutic mechanisms of deep brain stimulation. Future work will explore the feasibility of using deep brain stimulators for recording neural EIT to allow patient-specific mapping of subcortical pathways.

The noise levels used for simulation in this work include both in-vivo physiological noise and artificial multiplicative noise which arises from the source of the probe current. The contribution of the physiological noise can be minimised by imaging using frequencies which maximise the ratio of the impedance change to the background physiological noise. The multiplicative noise is magnified by the electrode impedance; future experiments will need to consider strategies to minimise the effect of this multiplicative noise. Fortunately for clinical applications, the electrode impedances for implanted DBS electrodes (around 10 kΩ at 1 kHz (Cogan, 2008)) are much lower than the impedances of the NeuroNexus arrays simulated here (around 600 kΩ at 1 kHz). For microelectrode arrays, other strategies such as coating the electrode surfaces with a low-impedance conductive polymer such as PEDOT can also be used to lower electrode impedances (Gerwig et al., 2012).

Acknowledgement

The authors would like to acknowledge Natalie Zeater, Paul Martin, Alexsander Pietersen, and Xin Cheng for their assistance in providing the electrophysiological data and ex vivo histology. This work was supported by the Australian National Health & Medical Research Council Project grant number 1042609; the Australian Research Council Centre of Excellence for Integrative Brain Function (ARC Centre Grant CE140100007), and a Faculty of Engineering Mid Career Researcher Grant and the Australian Institute for Nanoscale Science and Technology at The University of Sydney. The authors declare no competing financial interests.

Appendix A. Supplementary data

Supplementary data to this article can be found online at https://doi.org/10.1016/j.neuroimage.2019.05.023.

References

Adler, A., Boyle, A., Crabb, M.G., Gagnon, H., Grychtol, B., Lesparre, N., Lionheart, W.R.B., 2015. EIDORS v3.8. https://doi.org/10.5281/zenodo.17559.

Aristovich, K.Y., dos Santos, G.S., Packham, B.C., Holder, D.S., 2014. A method for reconstructing tomographic images of evoked neural activity with electrical impedance tomography using intracranial planar arrays. Physiol. Meas. 35 (6), 1095. http://stacks.iop.org/0967-3334/35/i=6/a=1095.

Aristovich, K.Y., Packham, B.C., Koo, H., dos Santos, G.S., McEvoy, A., Holder, D.S., 2016. Imaging fast electrical activity in the brain with electrical impedance tomography. Neuroimage 124, 204–213. https://doi.org/10.1016/j.neuroimage.2015.08.071.

Bayford, R.H., 2006. Bioimpedance tomography (electrical impedance tomography). Annu. Rev. Biomed. Eng. 8, 63–91.

Benabid, A.L., Pollak, P., Gao, D., Hoffmann, D., Limousin, P., Gay, E., Payen, I., Benazzouz, A., 1996. Chronic electrical stimulation of the ventralis intermedius nucleus of the thalamus as a treatment of movement disorders. J. Neurosurg. 84 (2), 203–214.

Birdno, M.J., Grill, W.M., 2008. Mechanisms of deep brain stimulation in movement disorders as revealed by changes in stimulus frequency. Neurotherapeutics 5 (1), 14–25.

Brummer, S., Turner, M., 1977. Electrical stimulation with Pt electrodes: II-estimation of maximum surface redox (theoretical non-gassing) limits. IEEE (Inst. Electr. Electron. Eng.) Trans. Biomed. Eng. 24 (5), 440–443.

Butson, C.R., McIntyre, C.C., 2008. Current steering to control the volume of tissue activated during deep brain stimulation. Brain Stimul.: Basic Transl. Clin. Res. Neuromodul. 1 (1), 7–15.

Buzsáki, G., Anastassiou, C.A., Koch, C., 2012. The origin of extracellular fields and currents - EEG, ECoG, LFP and spikes. Nat. Rev. Neurosci. 13, 407. https://doi.org/10.1038/nrn3241.

Cheney, M., Isaacson, D., Newell, J.C., Simske, S., Goble, J., 1990. NOSER: an algorithm for solving the inverse conductivity problem. Int. J. Imaging Syst. Technol. 2 (2), 66–75.

Cheong, S.K., Tailby, C., Solomon, S.G., Martin, P.R., 2013. Cortical-like receptive fields in the lateral 679 geniculate nucleus of marmoset monkeys. J. Neurosci. 33, 6864–6876.

Cogan, S.F., 2008. Neural stimulation and recording electrodes. Annu. Rev. Biomed. Eng. 10, 275–309.

Cogan, S.F., Plante, E.J.T.D., Smirnov, A., Shire, D.B., Gingerich, M., Rizzo, J.F., 2009. Sputtered iridium oxide films for neural stimulation electrodes. J. Biomed. Mater. Res. B Appl. Biomater. 89 (2), 353–361.

Contarino, M.F., Bour, L.J., Verhagen, R., Lourens, M.A., de Bie, R.M., van den Munckhof, P., Schuurman, P., 2014. Directional steering: a novel approach to deep brain stimulation. Neurology 83 (13), 1163–1169.

Couto, J., Grill, W.M., 2016. Kilohertz frequency deep brain stimulation is ineffective at regularizing the firing of model thalamic neurons. Front. Comput. Neurosci. 10, 22.

Davidson, J., Wright, P., Ahsan, S., Robinson, R., Pomfrett, C., McCann, H., 2010. fEITER–a new EIT instrument for functional brain imaging. In: Journal of Physics: Conference Series, vol. 224. IOP Publishing, 012025.

Eiber, C.D., Lovell, N.H., Suaning, G.J., 2013. Attaining higher resolution visual prosthetics: a review of the factors and limitations. J. Neural Eng. 10 (1), 011002.

Eiber, C.D., Rahman, A.S., Pietersen, A.N.J., Zeater, N., Dreher, B., Solomon, S.G., Martin, P.R., 2018. Receptive field properties of koniocellular on/off neurons in the lateral geniculate nucleus of marmoset monkeys. J. Neurosci. 38 (48), 10384–10398.

Faulkner, M., Jehl, M., Aristovich, K., Avery, J., Witkowska-Wrobel, A., Holder, D., 2017. Optimisation of current injection protocol based on a region of interest. Physiol. Meas. 38 (6), 1158. http://stacks.iop.org/0967-3334/38/i=6/a=1158.

Faulkner, M., Hannan, S., Aristovich, K., Avery, J., Holder, D., 2018a. Feasibility of imaging evoked activity throughout the rat brain using electrical impedance tomography. Neuroimage 178, 1–10. https://doi.org/10.1016/j.neuroimage.2018.05.022.

Faulkner, M., Hannan, S., Aristovich, K.Y., Avery, J., Holder, D.S., 2018b. Characterising the frequency response of impedance changes during evoked physiological activity in the rat brain. Physiol. Meas. 39 (3).

Gabriel, C., Peyman, A., Grant, E.H., 2009. Electrical conductivity of tissue at frequencies below 1 MHz. Phys. Med. Biol. 54 (16), 4863. http://stacks.iop.org/0031-9155/54/i=16/a=002.

Gerwig, R., Fuchsberger, K., Schroeppel, B., Link, G.S., Heusel, G., Kraushaar, U., Schuhmann, W., Stett, A., Stelzle, M., 2012. PEDOT-CNT composite microelectrodes for recording and electrostimulation applications: fabrication, morphology, and electrical properties. Front. Neuroeng. 5 (8).

Gippert, S.M., Switala, C., Bewernick, B.H., Kayser, S., Bräuer, A., Coenen, V.A., Schlaepfer, T.E., 2017. Deep brain stimulation for bipolar disorder–review and outlook. CNS Spectr. 22 (3), 254–257.

Grech, R., Cassar, T., Muscat, J., Camilleri, K.P., Fabri, S.G., Zervakis, M., Xanthopoulos, P., Sakkalis, V., Vanrumste, B., 2008. Review on solving the inverse problem in EEG source analysis. J. NeuroEng. Rehabil. 5 (1), 25.

Hansen, P.C., 2007. Regularization tools version 4.0 for Matlab 7.3. Numer. Algorithm. 46 (2), 189–194. https://doi.org/10.1007/s11075-007-9136-9. https://doi.org/10.1007/s11075-007-9136-9.

Histed, M., Bonin, V., Reid, R., 2009. Direct activation of sparse, distributed populations of cortical neurons by electrical microstimulation. Neuron 63 (4), 508–522. https://www.ncbi.nlm.nih.gov/pubmed/19709632.

Jehl, M., Aristovich, K., Faulkner, M., Holder, D., 2016. Are patient specific meshes required for EIT head imaging? Physiol. Meas. 37 (6), 879. http://stacks.iop.org/0967-3334/37/i=6/a=879.

Jeong, W.C., Sajib, S.Z., Kim, H.J., Kwon, O.I., 2014. Focused current density imaging using internal electrode in magnetic resonance electrical impedance tomography (MREIT). IEEE (Inst. Electr. Electron. Eng.) Trans. Biomed. Eng. 61 (7), 1938–1946.

Kajikawa, Y., Schroeder, C.E., 2011. How local is the local field potential? Neuron 72 (5), 847–858.

Liston, A., Bayford, R., Holder, D., 2012. A cable theory based biophysical model of resistance change in crab peripheral nerve and human cerebral cortex during neuronal depolarisation: implications for electrical impedance tomography of fast neural activity in the brain. Med. Biol. Eng. Comput. 50 (5), 425–437. https://doi.org/10.1007/s11517-012-0901-0.

Liu, A., Joe, B., 1994. Relationship between tetrahedron shape measures. BIT Numer. Math. 34 (2), 268–287. https://doi.org/10.1007/BF01955874.

Makarov, V.A., Makarova, J., Herreras, O., 2010. Disentanglement of local field potential sources by independent component analysis. J. Comput. Neurosci. 29 (3), 445–457.

Makarova, J., Ortuño, T., Korovaichuk, A., Cudeiro, J., Makarov, V.A., Rivadulla, C., Herreras, O., 2014. Can pathway-specific LFPs be obtained in cytoarchitectonically complex structures? Front. Syst. Neurosci. 8, 66. http://doi.org/10.3389/fnsys.2014.00066.

Malone, E., Jehl, M., Arridge, S., Betcke, T., Holder, D., 2014. Stroke type differentiation using spectrally constrained multifrequency eit: evaluation of feasibility in a realistic head model. Physiol. Meas. 35 (6).

Mayberg, H.S., Lozano, A.M., Voon, V., McNeely, H.E., Seminowicz, D., Hamani, C., Schwalb, J.M., Kennedy, S.H., 2005. Deep brain stimulation for treatment-resistant depression. Neuron 45 (5), 651–660.

McCreery, D.B., Agnew, W.F., Yuen, T.G.H., Bullara, L., 1990. Charge density and charge per phase as cofactors in neural injury induced by electrical stimulation. IEEE Trans. Biomed. Eng. 37 (10), 996–1001.

Miocinovic, S., Somayajula, S., Chitnis, S., Vitek, J.L., 2013. History, applications, and mechanisms of deep brain stimulation. JAMA Neurology 70 (2), 163–171.

Oh, T., Gilad, O., Ghosh, A., Schuettler, M., Holder, D.S., 2011. A novel method for recording neuronal depolarization with recording at 125–825 Hz: implications for imaging fast neural activity in the brain with electrical impedance tomography. Med. Biol. Eng. Comput. 49 (5), 593–604.

Paxinos, G., Watson, C., Petrides, M., Rosa, M., Tokuno, H., 2012. The Marmoset Brain in Stereotaxic Coordinates. Academic Press.

Pietersen, A.N.J., Cheong, S.K., Solomon, S.G., Tailby, C., Martin, P.R., 2014. Temporal response properties of koniocellular (blue-on and blue-off) cells in marmoset lateral geniculate nucleus. J. Neurophysiol. 112 (6), 1421–1438. https://doi.org/10.1152/jn.00077.2014 pMID: 24920024. https://doi.org/10.1152/jn.00077.2014.

Reilly, J.P., 2002. Neuroelectric mechanisms applied to low frequency electric and magnetic field exposure guidelines part I: sinusoidal waveforms. Health Phys. 83 (3), 341–355.

Rose, T., Robblee, L., 1990. Electrical stimulation with Pt electrodes. VIII. Electrochemically safe charge injection limits with 0.2 ms pulses (neuronal application). IEEE (Inst. Electr. Electron. Eng.) Trans. Biomed. Eng. 37 (11), 1118–1120.

Sahin, M., Tie, Y., 2007. Non-rectangular waveforms for neural stimulation with practical electrodes. J. Neural Eng. 4 (3), 227. http://stacks.iop.org/1741-2552/4/i=3/a=008.

Sturm, V., Lenartz, D., Koulousakis, A., Treuer, H., Herholz, K., Klein, J.C., Klosterkötter, J., 2003. The nucleus accumbens: a target for deep brain stimulation in obsessive–compulsive-and anxiety-disorders. J. Chem. Neuroanat. 26 (4), 293–299.

Tailby, C., Dobbie, W.J., Solomon, S.G., Szmajda, B.A., Hashemi-Nezhad, M., Forte, J.D., Martin, P.R., 2010. Receptive field asymmetries produce color-dependent direction selectivity in primate lateral geniculate nucleus. J. Vis. 10 (8), 1. https://doi.org/10.1167/10.8.1. https://doi.org/10.1167/10.8.1.

Tamma, F., Caputo, E., Chiesa, V., Egidi, M., Locatelli, M., Rampini, P., Cinnante, C., Pesenti, A., Priori, A., 2002. Anatomo-clinical correlation of intraoperative stimulation-induced side-effects during HF-DBS of the subthalamic nucleus. Neurol. Sci. 23 (2), s109–s110.

Tan, S.K., Hartung, H., Schievink, S., Sharp, T., Temel, Y., 2013. High-frequency stimulation of the substantia nigra induces serotonin-dependent depression-like behavior in animal models. Biol. Psychiatry 73 (2) e1–e3.

White, A.J., Wilder, H.D., Goodchild, A.K., Sefton, A.J., Martin, P.R., 1998. Segregation of receptive field properties in the lateral geniculate nucleus of a new-world monkey, the marmoset callithrix jacchus. J. Neurophysiol. 80 (4), 2063–2076.

Witkowska-Wrobel, A., Aristovich, K., Faulkner, M., Avery, J., Holder, D., 2018. Feasibility of imaging epileptic seizure onset with EIT and depth electrodes. Neuroimage 173, 311–321.

Łeski, S., Lindén, H., Tetzlaff, T., Pettersen, K.H., Einevoll, G.T., 2013. Frequency dependence of signal power and spatial reach of the local field potential. PLoS Comput. Biol. 9 (7), e1003137.